Supplementary Information for

Multifunctional vortex magnetic tunnel junctions with optical and radio-frequency inputs for neuromorphic computing

Felix Oberbauer, Tristan Joachim Winkel, Clara C. Wanjura, Maksim Steblii, John Justice, Jakob Walowski, Tim Böhnert, Eoin Russell, Farshad Moradi, Ricardo Ferreira, Brian Corbett, Markus Münzenberg, Tahereh Sadat Parvini

---

Contents

Supplementary Note 1.
Device-to-device reproducibility of the zero-bias TMS response and diameter scaling

Supplementary Note 2.
Reproducibility of the bias-enhanced (bTMS) response

Supplementary Note 3.
Coincident magnetic switching of resistance and laser-induced voltage, and spikes during reversal

Supplementary Note 4.
Bias dependence of the P/AP resistances and the tunnel magnetoresistance ratio

Supplementary Note 5.
Laser-induced modulation of the P/AP resistances under combined optical and electrical drive

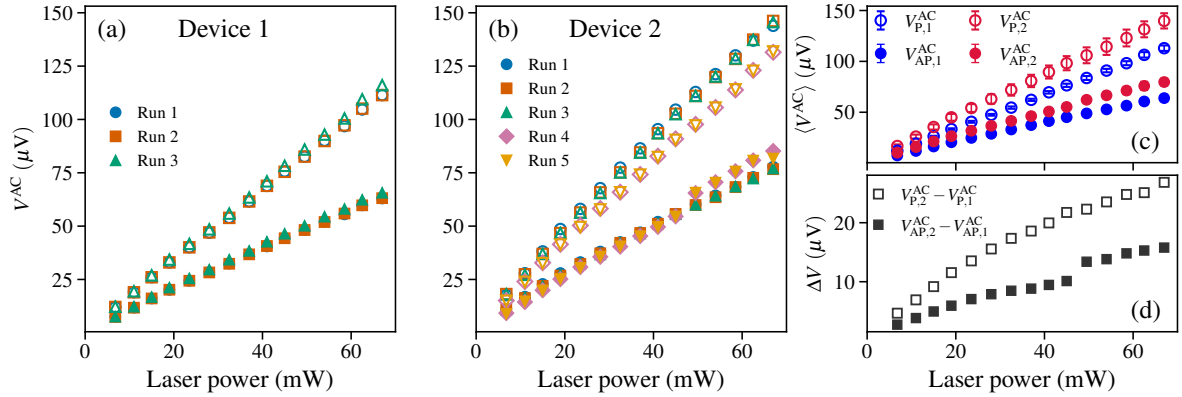
Supplementary Note 6.
Linear power scaling of the bias-enhanced laser-induced voltage at fixed dc bias

Supplementary Note 7.
Optical delivery and thermal simulation of focused VCSEL addressing

Supplementary References.
Supplementary References

Supplementary Note 1. Device-to-device reproducibility of the zero-bias TMS response and diameter scaling

Within- and between-device reproducibility at $d = 800\,\mathrm{nm}$. As a first quantitative test of the reproducibility of the tunnel magneto-Seebeck (TMS) response, we performed independent laser-power sweeps on two nominally identical $d = 800\,\mathrm{nm}$ vortex magnetic tunnel junctions (MTJs), acquiring $N = 3$ sweeps on Device 1 and $N = 5$ sweeps on Device 2 over several months. Supplementary Fig. 1 summarizes this analysis. Panels (a,b) overlay every individual run of each



Supplementary Fig. 1. Within- and between-device reproducibility of the optothermal TMS response for two nominally identical $d = 800$ nm vortex MTJs. (a,b) Individual laser-power sweeps for Device 1 ($N = 3$ runs) and Device 2 ($N = 5$ runs); open and filled markers denote $V_{\mathrm{P}}^{\mathrm{AC}}$ and $V_{\mathrm{AP}}^{\mathrm{AC}}$ at $B_{\parallel} = \pm 30$ mT; different colours and shapes label distinct runs of the same device. (c) Run-averaged $V_{\mathrm{P}}^{\mathrm{AC}}$ (open) and $V_{\mathrm{AP}}^{\mathrm{AC}}$ (filled) for Device 1 (blue) and Device 2 (red); error bars are the run-to-run sample standard deviation. (d) Device-to-device signed difference $\Delta V = V_2 - V_1$ of the run-averaged voltages, for both magnetic states.

device, with open and filled markers denoting $V_{\mathrm{P}}^{\mathrm{AC}}$ and $V_{\mathrm{AP}}^{\mathrm{AC}}$ at $B_{\parallel} = \pm 30$ mT. Within each device, all runs collapse onto a single linear trace to within the marker size, so single-device drift, optical-alignment variations and lock-in noise are negligible. Panel (c) gives the run-averaged $V_{\mathrm{P}}^{\mathrm{AC}}$ and $V_{\mathrm{AP}}^{\mathrm{AC}}$ for each device; the run-to-run sample standard deviation is of order 1 μV across the full power range, so the per-device mean is well defined.

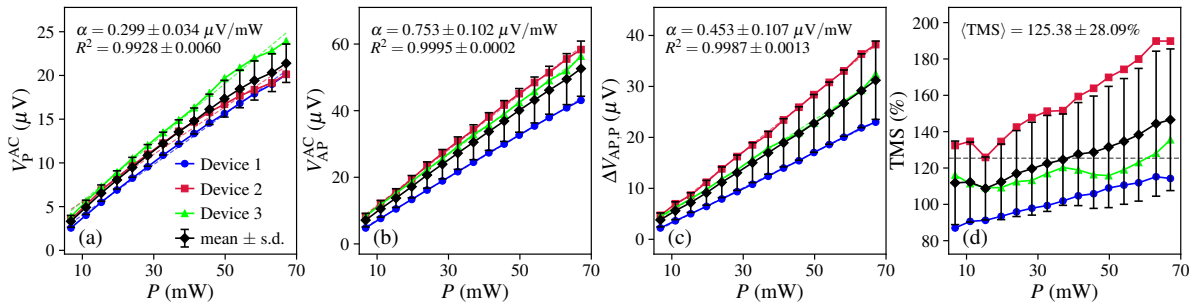
A small but systematic offset between the two devices is resolved in panel (c) and quantified in panel (d) by the signed difference $\Delta V = V_2 - V_1$ of the device-averaged voltages. ΔV scales approximately linearly with laser power and remains below ∼30 μV at $P_{\mathrm{laser}} = 67$ mW for both magnetic states. This residual offset is consistent with fabrication-induced differences in optical absorption, top-contact transparency, MgO microstructure and substrate thermal coupling, all of which feed into the steady-state temperature difference ΔT and the spin-dependent Seebeck coefficients $S_{\mathrm{P/AP}}$. The qualitative response—linear power scaling, hysteretic switching between the parallel (P) and antiparallel (AP) states, and the sign and ordering of $V_{\mathrm{P}}^{\mathrm{AC}}$ and $V_{\mathrm{AP}}^{\mathrm{AC}}$—is identical for both devices, so the diameter-dependent trends and TMS ratios reported in Fig. 2 of the main text are not artefacts of single-device variability.

Diameter scaling. To extend the analysis across diameters, we measured three nominally identical vortex MTJs for each of $d = 600$ nm, 800 nm and 1000 nm. Repeated traces at the same laser power were averaged within each device, and statistics were computed over the laser powers common to all devices within a diameter group. For each device we extract $V_{\mathrm{P}}^{\mathrm{AC}}$ and $V_{\mathrm{AP}}^{\mathrm{AC}}$ from the plateau regions, the contrast $\Delta V_{\mathrm{AP,P}} = V_{\mathrm{AP}}^{\mathrm{AC}} - V_{\mathrm{P}}^{\mathrm{AC}}$, and the TMS ratio defined as in the main text.

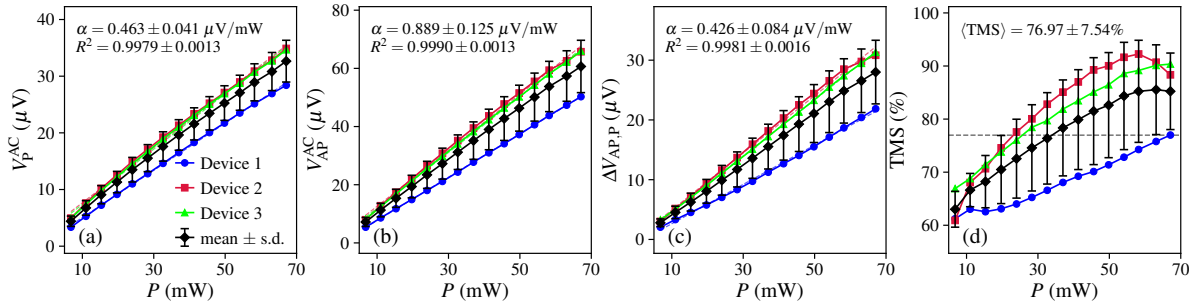
Supplementary Figs. 2–4 show approximately linear laser-power scaling of $V_{\mathrm{P}}^{\mathrm{AC}}$, $V_{\mathrm{AP}}^{\mathrm{AC}}$ and $\Delta V_{\mathrm{AP,P}}$ at all three diameters. The device-averaged TMS ratio decreases from 125 ± 28 % at $d = 600$ nm to 77.0 ± 7.5 % at 800 nm and 54.5 ± 4.4 % at 1000 nm, confirming the diameter-dependent trend reported in the main text.

Supplementary Note 2. Reproducibility of the bias-enhanced (bTMS) response

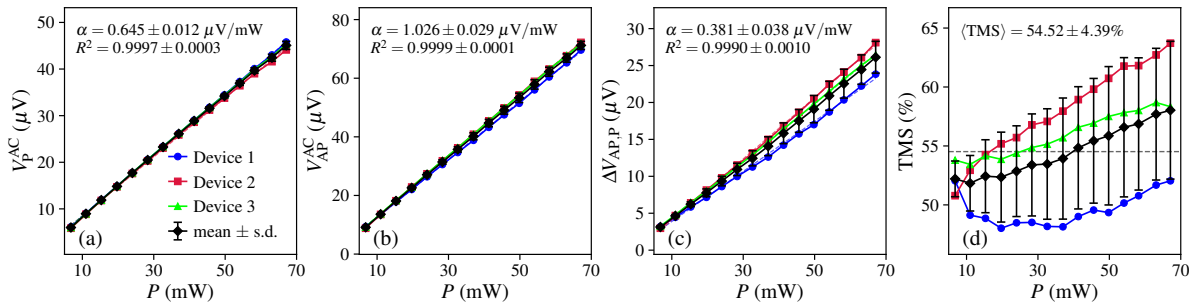
Supplementary Note 1 dealt with the zero-bias case. The bias-enhanced TMS (bTMS) regime, in which laser heating and a finite dc bias I_{bias} act simultaneously, is a stricter test: a small



Supplementary Fig. 2. Device-to-device reproducibility of the optothermal TMS response, $d = 600$ nm. (a,b) $V_{\mathrm{P}}^{\mathrm{AC}}$ and $V_{\mathrm{AP}}^{\mathrm{AC}}$ versus calibrated laser power. (c) Contrast $\Delta V_{\mathrm{AP,P}}$. (d) TMS ratio. Coloured symbols are individual devices; black diamonds and error bars are the mean ± sample standard deviation across $N = 3$ devices; dashed lines in (a–c) are independent linear fits to each device. Device-averaged TMS ratio: $\langle \mathrm{TMS} \rangle = 125 \pm 28\,\%$.



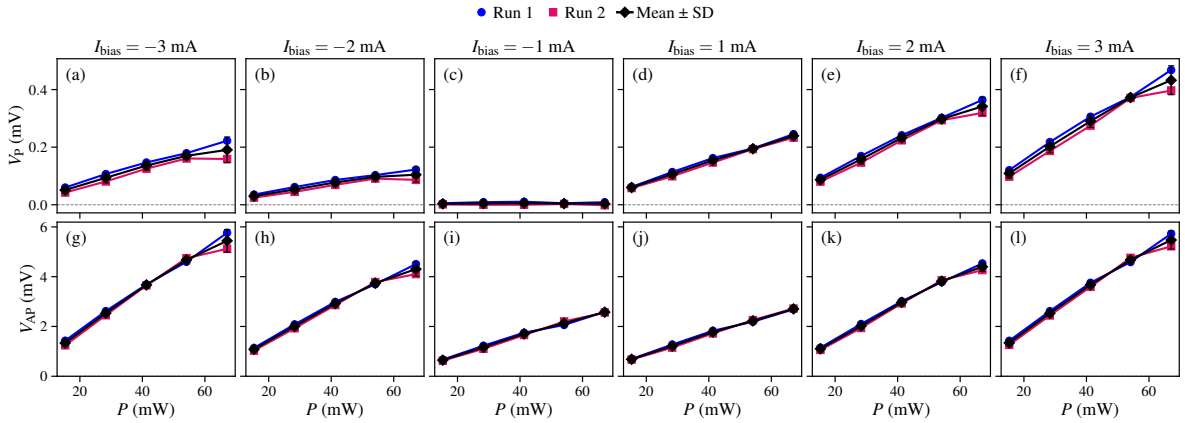
Supplementary Fig. 3. Device-to-device reproducibility of the optothermal TMS response, $d = 800$ nm. Same analysis as Supplementary Fig. 2, for $N = 3$ devices. Device-averaged TMS ratio: $\langle \mathrm{TMS} \rangle = 77.0 \pm 7.5\,\%$.



Supplementary Fig. 4. Device-to-device reproducibility of the optothermal TMS response, $d = 1000$ nm. Same analysis as Supplementary Fig. 2, for $N = 3$ devices. Device-averaged TMS ratio: $\langle \mathrm{TMS} \rangle = 54.5 \pm 4.4\,\%$.

drift in optical alignment, contact resistance or barrier microstructure no longer simply rescales a single slope, but reshapes the entire $\Delta V_{\mathrm{AC}}(I_{\mathrm{bias}}, P_{\mathrm{laser}})$ map. The primary characterization uses $d = 800$ nm devices—the diameter already documented at zero bias—and is complemented by independent device-to-device data at $d = 600$ nm. All measurements use the same lock-in detection as in Fig. 4 of the main text; the laser-induced voltages in the P and AP states, denoted $V_{\mathrm{P}}^{\mathrm{AC}}$ and $V_{\mathrm{AP}}^{\mathrm{AC}}$ here and $\Delta V_{\mathrm{AC}}^{\mathrm{P}}$ and $\Delta V_{\mathrm{AC}}^{\mathrm{AP}}$ in the main text, are read off at $B_{\parallel} = \pm 30$ mT. We probe two complementary axes of variability: a temporal axis, by re-measuring a single device on different days, and a spatial axis, by comparing nominally identical devices at different locations on the same chip.

Run-to-run reproducibility, single $d = 800$ nm device. Supplementary Fig. 5 shows $V_{\mathrm{P}}^{\mathrm{AC}}$ and $V_{\mathrm{AP}}^{\mathrm{AC}}$ for one $d = 800$ nm junction measured on two different days, plotted against laser power for



Supplementary Fig. 5. Run-to-run reproducibility of the bTMS response, single $d = 800$ nm device. V_P^{AC} (top row) and V_{AP}^{AC} (bottom row) versus laser power, for the indicated dc bias currents. Coloured markers are independent measurement runs on different days; black diamonds and error bars give the run-averaged mean ± sample standard deviation. Repeats at the same (P_{laser}, I_{bias}) within a run are averaged before the statistics are computed.

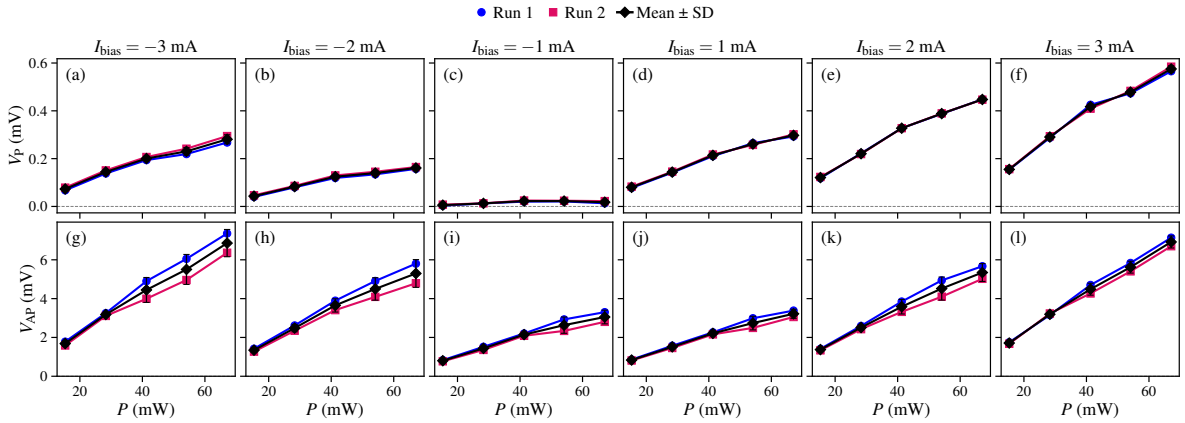
each dc bias. The two runs overlap to within the marker size across the entire (P_{laser}, I_{bias}) range, including the near-vanishing condition at $I_{bias} \approx -1$ mA, where the bTMS ratio is most sensitive to any drift (Fig. 4 of the main text). Day-to-day variations in alignment, lock-in calibration and ambient conditions therefore contribute negligibly to the bTMS uncertainty.

Device-to-device reproducibility. We compared nominally identical junctions at different locations on the chip: a first pair of $d = 600$ nm junctions (Supplementary Fig. 6), a pair of $d = 800$ nm junctions (Supplementary Fig. 7) and a second, independent pair of $d = 600$ nm junctions (Supplementary Fig. 8), covering four distinct $d = 600$ nm junctions in total. Repeated measurements are first averaged within each device, as in Supplementary Fig. 5. For both diameters, the devices reproduce the same qualitative response: V_P^{AC} and V_{AP}^{AC} scale approximately linearly with laser power at every fixed I_{bias}, consistent with $\Delta T \propto P_{laser}$ and with the linear power scaling at fixed bias (Supplementary Note 6), and the sign, magnitude and bias-current ordering of the response are preserved. The per-device traces cluster tightly at every bias current, and the residual offset between devices is comparable to the device-to-device spread at zero bias (Supplementary Note 1), so adding a finite bias does not introduce additional variability.

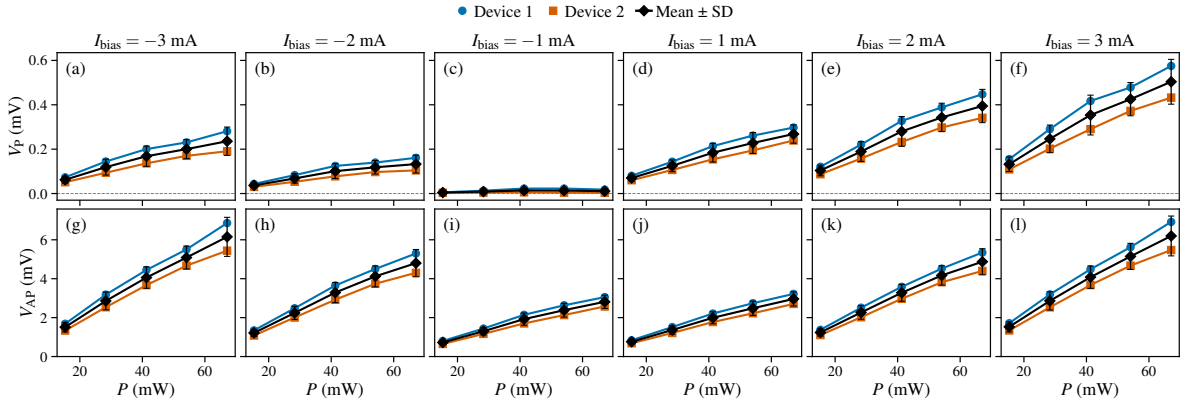
Taken together, Supplementary Figs. 5–8 show that the bTMS response is reproducible along both the temporal and the spatial axis and for both diameters tested. The cubic bias dependence that underpins the bTMS operating mode (Figs. 4 and 5 of the main text) is therefore a property of the junction stack rather than of a single nanopillar. This supports the use of one measured response map for all junctions in the network simulations of the main text, although device-to-device variation was not included in those simulations.

Supplementary Note 3. Coincident magnetic switching of resistance and laser-induced voltage, and spikes during reversal

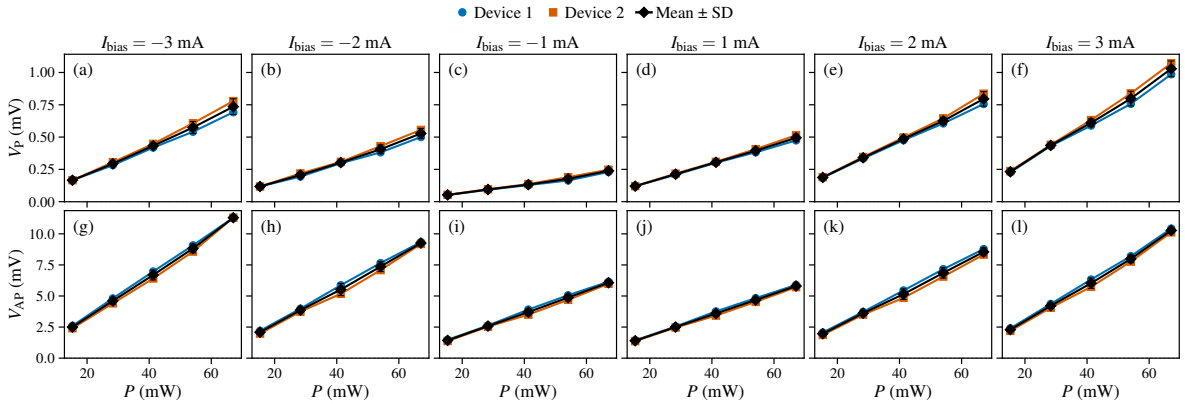
In the bias-enhanced measurements, the dc resistance $R(B)$ and the laser-induced voltage $\Delta V_{AC}(B)$ are recorded simultaneously. Both signals switch at the same fields, with different amplitudes (Supplementary Fig. 9), confirming their common magnetic origin; each junction therefore offers two readout channels of its magnetic state, its resistance and its laser-induced voltage. At fixed $P_{laser} = 67$ mW, increasing $|I|$ increases $|\Delta V_{AC}|$, as expected for the bias-enhanced signal, which contains a bias-dependent thermoelectric term and a resistive term $\Delta R\, I$ (main text) [1, 2].



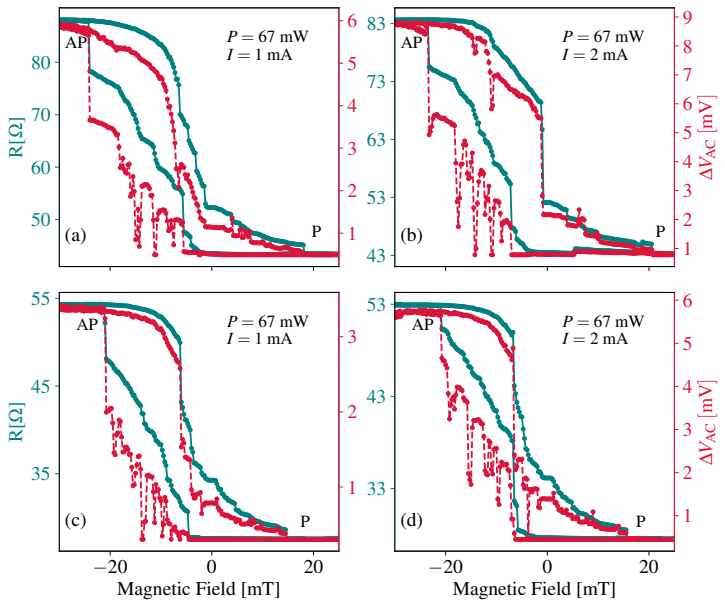
Supplementary Fig. 6. Device-to-device reproducibility of the bTMS response, $d = 600$ nm (first device pair). V_P^{AC} (top row) and V_{AP}^{AC} (bottom row) versus laser power, for the indicated dc bias currents. Coloured markers are independent devices at different chip locations; black diamonds and error bars give the across-device mean ± sample standard deviation. Within each device, repeated measurements and runs are averaged before the across-device statistic is computed.



Supplementary Fig. 7. Device-to-device reproducibility of the bTMS response, $d = 800$ nm. Same conventions as Supplementary Fig. 6, applied to two $d = 800$ nm devices at different chip locations.



Supplementary Fig. 8. Device-to-device reproducibility of the bTMS response, $d = 600$ nm (second device pair). Same conventions as Supplementary Fig. 6, applied to a second, independent pair of $d = 600$ nm devices located elsewhere on the chip. Together with Supplementary Fig. 6, the comparison covers four distinct $d = 600$ nm junctions.



Supplementary Fig. 9. Laser-induced voltage and resistance versus in-plane magnetic field. ΔV_{AC} and R, recorded simultaneously under laser heating and dc bias, for vortex MTJs with (a,b) $d = 600\,\mathrm{nm}$ and (c,d) $d = 800\,\mathrm{nm}$. Sharp spikes in ΔV_{AC} accompany the resistance steps during reversal (Supplementary Note 3).

During reversal, the discrete steps in $R(B)$ are accompanied by sharp spikes in $\Delta V_{\mathrm{AC}}(B)$ (Supplementary Fig. 9). We tentatively associate these steps and spikes with Barkhausen-like jumps of the vortex-state free layer, such as the depinning of the vortex core from defects [3, 4]. Because the spikes coincide with steps in $R(B)$, they are most likely dominated by abrupt changes of the resistive term $\Delta R\, I$. Moreover, the field is stepped while the signal is detected with a lock-in amplifier, so an abrupt resistance step can also produce a transient in the lock-in output. Time-resolved measurements are therefore needed to establish the intrinsic shape and duration of these events and to assess their use for event-driven neuromorphic signalling.

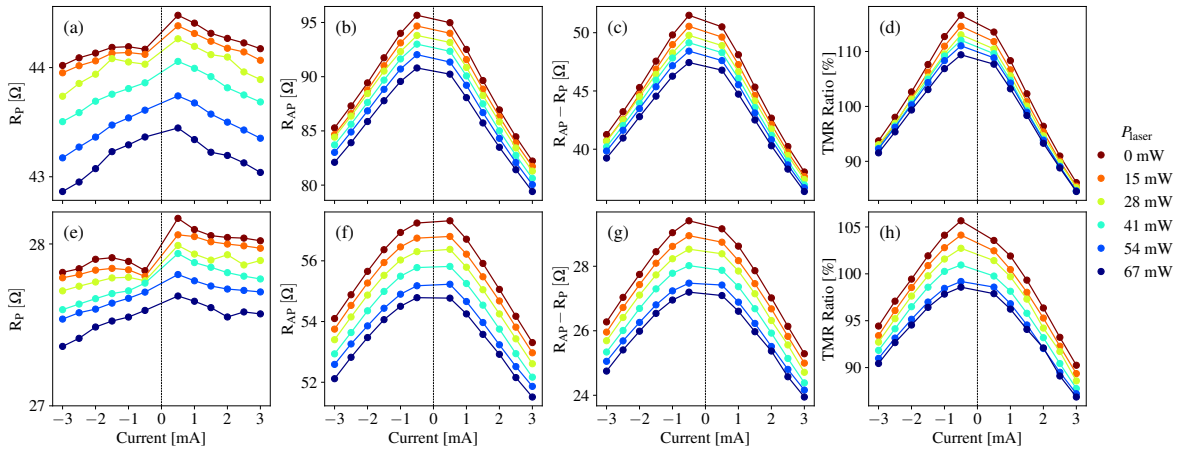
Supplementary Note 4. Bias dependence of the P/AP resistances and the tunnel magnetoresistance ratio

Supplementary Fig. 10 shows R_{P}, R_{AP} and the tunnel magnetoresistance (TMR) ratio, $\mathrm{TMR} = (R_{\mathrm{AP}} - R_{\mathrm{P}})/\min(|R_{\mathrm{P}}|, |R_{\mathrm{AP}}|)$ [5], as functions of dc bias for several laser powers. The TMR reaches $\sim$120 % for $d = 600\,\mathrm{nm}$ and $\sim$105 % for $d = 800\,\mathrm{nm}$. Smaller pillars have a larger resistance in both states, as expected from the smaller junction area ($R \propto 1/d^2$ at a constant resistance–area product).

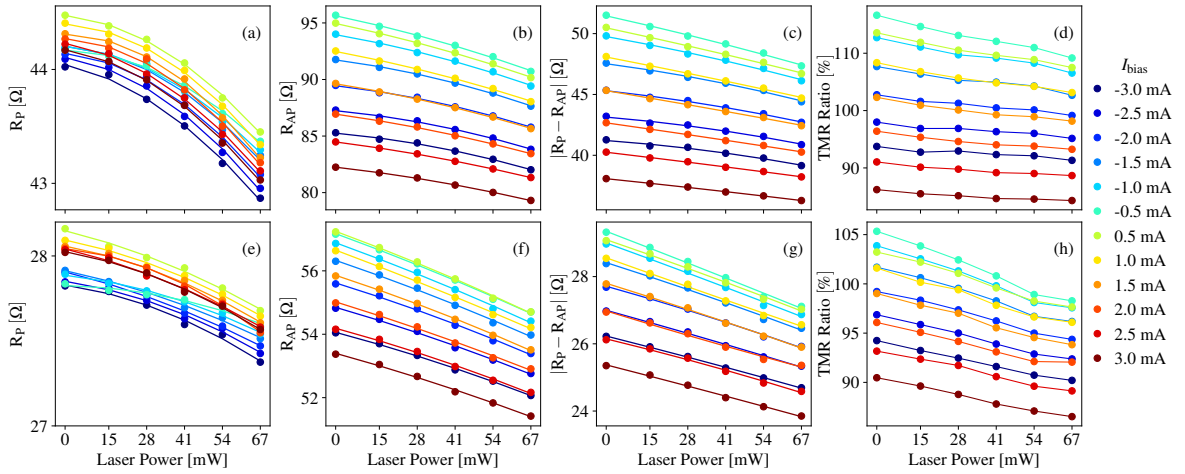
R_{P} decreases almost linearly with bias, indicating weakly nonlinear transport dominated by coherent tunnelling in the parallel state. R_{AP} instead shows a dome-shaped bias dependence: it is nearly constant at low bias and decreases at higher currents. This decrease is the typical bias dependence of the antiparallel state in MgO-based junctions; at the highest currents, Joule heating and spin-transfer torque acting on the free-layer vortex may also contribute.

Supplementary Note 5. Laser-induced modulation of the P/AP resistances under combined optical and electrical drive

The effect of laser heating on transport is seen most directly in Supplementary Fig. 11, where R_{P}, R_{AP} and the TMR are plotted against laser power at fixed bias. R_{AP} decreases almost linearly with laser power, consistent with the stronger temperature dependence of the antiparallel-state resistance, whereas R_{P} depends only weakly, and slightly nonlinearly, on laser power. The



Supplementary Fig. 10. P/AP-state resistance and TMR versus dc bias. R_P, R_{AP} and TMR versus dc bias for several laser powers; $d = 600\,\text{nm}$ (top row) and $d = 800\,\text{nm}$ (bottom row).



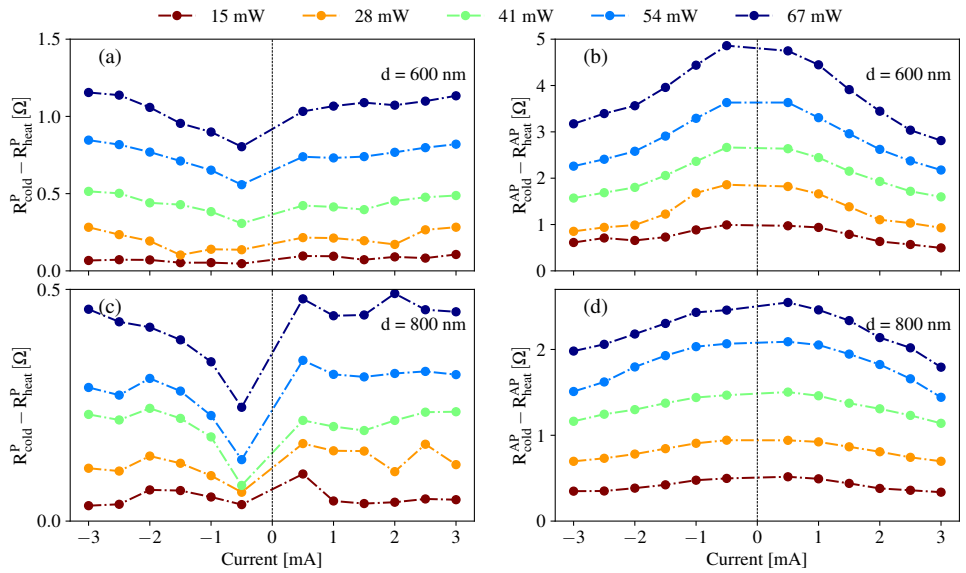
Supplementary Fig. 11. P/AP-state resistance and TMR versus laser power. R_P, R_{AP} and TMR versus laser power for several dc bias currents; $d = 600\,\text{nm}$ (top row) and $d = 800\,\text{nm}$ (bottom row).

asymmetry between the two magnetic states reflects their different spin-dependent transport.

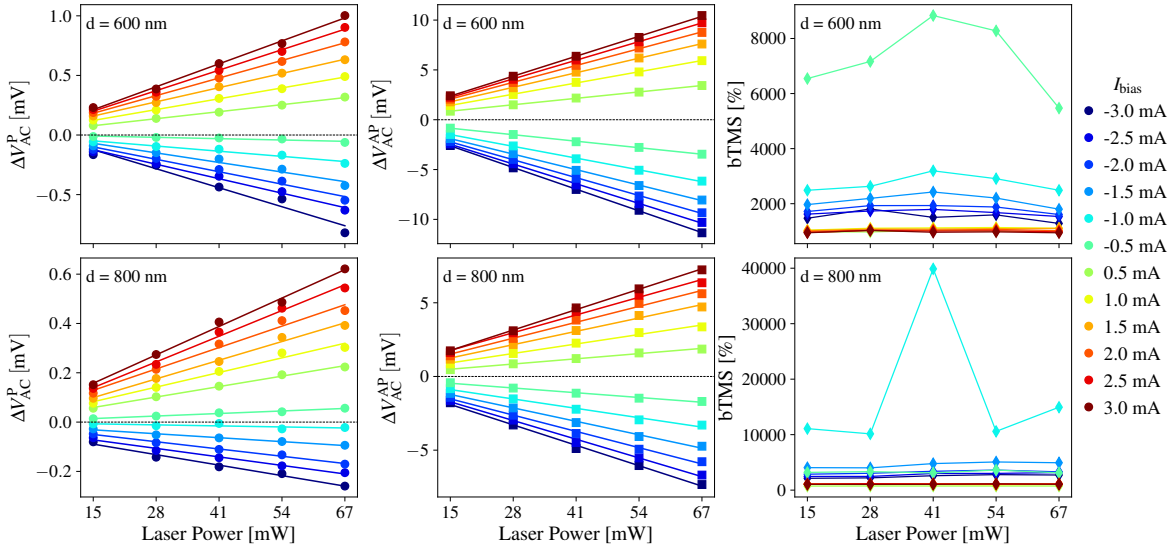
Supplementary Fig. 12 quantifies the heating-induced resistance change $\Delta R = R_{\text{cold}} - R_{\text{heat}}$ versus bias for both diameters and both magnetic states. This is the quantity that enters the resistive term $\Delta R\, I$ of the bias-enhanced signal (main text). ΔR_P stays small for all powers and currents, whereas ΔR_{AP} grows strongly with both $|I|$ and P_{laser}, most clearly for the $d = 600\,\text{nm}$ junction, whose larger resistance ($R \propto 1/d^2$) gives a larger absolute change for the same relative change. The resistive term therefore contributes mainly in the AP state and at high bias.

Supplementary Note 6. Linear power scaling of the bias-enhanced laser-induced voltage at fixed dc bias

Supplementary Fig. 13 shows that both $\Delta V_{\text{AC}}^{\text{P}}$ and $\Delta V_{\text{AC}}^{\text{AP}}$ increase approximately linearly with laser power at fixed bias. This is expected because both the thermoelectric term $S\,\Delta T$ and the resistive term $\Delta R\, I$ are proportional to the temperature rise for small heating, with $\Delta T \propto P_{\text{laser}}$. Plotted against bias at fixed power (Fig. 4 of the main text), the signal is instead distinctly nonlinear and well described by a cubic polynomial [1, 6]. This combination, linear in power and cubic in bias, is what we use for computing: each junction multiplies its optical input by an effective weight that depends nonlinearly on the bias current.



Supplementary Fig. 12. Laser-induced resistance modulation versus bias current. $\Delta R_m = R_m^{\mathrm{cold}} - R_m^{\mathrm{heat}}$ in the P and AP states ($m = \mathrm{P}, \mathrm{AP}$) versus dc bias I, for $d = 600\,\mathrm{nm}$ and $800\,\mathrm{nm}$; R_m^{cold} is taken at $P_{\mathrm{laser}} = 0$ and R_m^{heat} at the indicated laser powers.

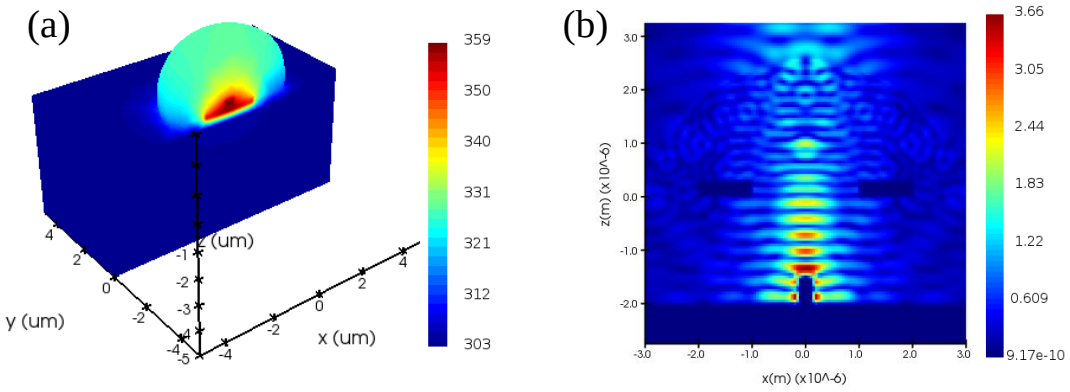


Supplementary Fig. 13. Bias-enhanced laser-induced voltage and bTMS ratio versus laser power. ΔV_{bias}, the laser-induced voltage denoted ΔV_{AC} in the main text, in the P and AP states and the bTMS ratio versus laser power for each dc bias; $d = 600\,\mathrm{nm}$ (top row) and $d = 800\,\mathrm{nm}$ (bottom row).

Supplementary Note 7. Optical delivery and thermal simulation of focused VCSEL addressing

Individual optical addressing of nanopillars in the bTMS mode requires focusing the light of a vertical-cavity surface-emitting laser (VCSEL) onto each junction; the experimental components, reflowed polydimethylglutarimide (PMGI) microlenses and a flip-chip-mounted VCSEL array, are shown in Fig. 6 of the main text. Here we summarize the supporting finite-element optical and thermal simulations.

In the simulations, a Gaussian beam is focused by a 6 µm-diameter hemispherical microlens onto a 200 nm-diameter nanopillar, representative of a scaled device, which strongly enhances the optical intensity at the nanopillar (Supplementary Fig. 14a). The resulting temperature rise,



Supplementary Fig. 14. Simulation of focused optical delivery and heating of a nanopillar. (a) Simulated optical-intensity cross-section for light focused onto a 200 nm-diameter nanopillar through a 6 µm-diameter hemispherical microlens (spatial axes in m; colour scale in arbitrary units). (b) Corresponding simulated steady-state temperature distribution around the nanopillar (axes in µm; colour scale in K); the ∼100 K rise quoted in the main text corresponds to focusing close to the optical wavelength.

set by optical absorption in the nanopillar stack and by heat dissipation into the surrounding materials (Supplementary Fig. 14b), reaches ∼100 K for ∼2 mW of incident power when the beam is focused close to the optical wavelength, which is the temperature rise used for bTMS operation.

This rise also sets the precision required for the optical power: closed-loop power stabilization at the 0.1–1 % level corresponds to temperature fluctuations of $\lesssim$1 K, a small fraction of the operating temperature rise.

Supplementary References

[1] Alexander Boehnke, Marius Milnikel, Marvin von der Ehe, Christian Franz, Vladyslav Zbarsky, Michael Czerner, Karsten Rott, Andy Thomas, Christian Heiliger, Günter Reiss, and Markus Münzenberg. On/off switching of bit readout in bias-enhanced tunnel magneto-Seebeck effect. *Sci. Rep.*, 5:8945, 2015. doi:10.1038/srep08945.

[2] Timo Kuschel, Michael Czerner, Jakob Walowski, Andy Thomas, Hans Werner Schumacher, Günter Reiss, Christian Heiliger, and Markus Münzenberg. Tunnel magneto-Seebeck effect. *J. Phys. D: Appl. Phys.*, 52(13):133001, 2019. doi:10.1088/1361-6463/aafa5f.

[3] M. Kuepferling, S. Zullino, A. Sola, B. Van de Wiele, G. Durin, M. Pasquale, K. Rott, G. Reiss, and G. Bertotti. Vortex dynamics in Co-Fe-B magnetic tunnel junctions in presence of defects. *J. Appl. Phys.*, 117(17):17E107, 2015. doi:10.1063/1.4908142.

[4] Felipe Bohn, Gianfranco Durin, Marcio Assolin Correa, Núbia Ribeiro Machado, Rafael Domingues Della Pace, Carlos Chesman, and Rubem Luis Sommer. Playing with universality classes of Barkhausen avalanches. *Sci. Rep.*, 8:11294, 2018. doi:10.1038/s41598-018-29576-3.

[5] Neha Jha, Anand Pariyar, Tahereh Sadat Parvini, Christian Denker, Pavan K. Vardhanapu, Gonela Vijaykumar, Arne Ahrens, T. Meyer, Michael Seibt, N. Atodiresei, Jagadeesh S. Moodera, Swadhin K. Mandal, and Markus Münzenberg. Interface-assisted room-temperature

magnetoresistance in Cu-phenalenyl-based magnetic tunnel junctions. *ACS Appl. Electron. Mater.*, 5(3):1471–1477, 2023. doi:10.1021/acsaelm.2c01428.

[6] Felix Oberbauer, Tristan Joachim Winkel, Tim Böhnert, Clara C. Wanjura, Marcel S. Claro, Luana Benetti, Ihsan Çaha, Francis Leonard Deepak, Farshad Moradi, Ricardo Ferreira, Markus Münzenberg, and Tahereh Sadat Parvini. Magnetic tunnel junctions driven by hybrid optical-electrical signals as a flexible neuromorphic computing platform. *Commun. Phys.*, 8:329, 2025. doi:10.1038/s42005-025-02257-0.